SCIENCE CHINA PRESS

SCIENCE CHINA Chemistry 2026 69(1): 362–370
https://doi.org/10.1007/s11426-025-2766-3

ARTICLES

H/F/Cl substituted naphthalenyl end-capped PM6 for high-performance organic solar cells

Tingfu Liu[1,2], Xuan Li[2,3], Jiaqing Liu[1,2], Yiming Li[2,3], Xiaomei Gao[3], Huajie Huang[1], Rong Huang[4], Qing Zhang[4], Meng Wang[1,2*], Haiyan He[1*] & Chang-Qi Ma[2*]

[1]College of Materials Science and Engineering, Hohai University, Nanjing 210098, China
[2]i-Lab & Printable Electronics Research Center, Suzhou Institute of Nano-Tech and Nano-Bionics, Chinese Academy of Sciences, Suzhou 215123, China
[3]College of Chemistry and Materials Science, Key Laboratory of Chemical Biology of Hebei Province, Hebei University, Baoding 071002, China
[4]Vacuum Interconnected Nanotech Workstation (Nano-X), Suzhou Institute of Nano-Tech and Nano-Bionics of Chinese Academy of Sciences, Suzhou 215123, China
*Corresponding authors (email: mwang2021@sinano.ac.cn; he.haiyan@hhu.edu.cn; cqma2011@sinano.ac.cn)

Received 14 March 2025; Accepted 12 May 2025; Published online 9 October 2025

Abstract Currently, the polymer PM6 stands out as one of the most efficient donor polymers in the field of organic solar cells, and many researchers are dedicated to further enhancing its photovoltaic performance. Among various strategies, the end-capping modification was a simple and effective way to minimize the undesired end-capping impurity groups and to narrow the molecular weight distribution of the final polymer donors. In this study, we systematically investigated the substitution effect of H, F, and Cl of the end-capping naphthyl group of the PM6 polymer on the photovoltaic performance. Compared to the naphthyl and fluoro-naphthyl group, the chloro-naphthyl moiety possesses a larger dipole moment, thereby enhancing the interaction between chloro-naphthyl end-capped PM6 with the small molecule acceptor, L8-BO, significantly reducing the π-π stacking distances between molecules and enhancing charge-carrier mobilities. Devices based on PM6-Cl:L8-BO exhibited appropriate phase separation, optimal molecular orientation, and minimal charge recombination. Consequently, the PM6-Cl:L8-BO-based device achieved an outstanding power conversion efficiency of 18.07%, with simultaneous enhancements in short-circuit current density (J_{SC}) and fill factor (FF). This was much higher than those of PM6-F:L8-BO-based (17.60%) and PM6-H:L8-BO-based (16.87%) devices. These results demonstrated that the modulation of end-capped atoms in PM6 could significantly improve the photovoltaic performance of organic solar cells and provide guidance for the design and synthesis of high-performance polymers.

Keywords organic solar cells, conjugated polymer, end-capping, donor-acceptor interactions, structure-property-performance relationship

1 Introduction

Organic solar cells (OSCs) have garnered widespread research attention due to their attractive features, such as solution processability, cost-effectiveness, and mechanical flexibility [1–4]. With the rapid development of non-fullerene acceptors (NFAs), the power conversion efficiency (PCE) of single-junction OSCs has continuously increased to over 20% [5]. However, compared to the extensive efforts in developing non-fullerene acceptors, research on polymer donor materials was relatively limited. In order to comprehensively adjust various components of the active layer and further improve the performance of OSC devices, it was necessary to design high-performance polymer donors to optimize the wettability of the polymer with the NFA molecules, thereby obtaining well-defined nanofiber structures and improving device performance. Currently, D-A conjugated-copolymers dominate the highest records of organic photovoltaic donor materials. Among the polymers reported so far, the most representative polymer donor is PM6, which exhibited excellent performance when blended with various NFAs [6]. Additionally, end-capping of polymers is an easy but effective method for modifying polymer molecules. In the case of PM6 synthesized by Stille coupling of organic bromide and stannane monomers, end-capping would reduce the bromo (–Br) and trimethylstannyl (–$SnMe_3$) groups of the PM6, which lowers the carrier traps [7]. Thus, end-capping of conjugated polymers could improve charge transport properties and the consequent short circuit current (J_{SC}) and PCE of the cells [8].

As a simple method to optimize donor materials, utilizing end-capping reagents to modify PM6 molecules has been proven effective in enhancing exciton dissociation, charge transport, and collection processes [8–12]. Recently, Huo *et al.* [13] used para-methoxyphenyl to end-cap PM6, resulting in single-end-capped and high-molecular-weight polymer PM6TPO. This polymer exhibited significantly enhanced crystallinity compared to PM6 and a notable reduction in non-radiative recombination voltage loss (V_{oc}^{nonrad}), thus achieving a lower energy loss. Therefore, the PCE of PM6TPO-based OSCs was higher than that of PM6-based devices, which was ascribed to the fact that the end-capping groups enhanced the miscibility between the donor and acceptor, thereby increasing and balancing the charge transport within the cells. Recently, we introduced crown ether as an end-capping group to modify the polymer donor PM6, synthesizing a series of end-capped polymer donors [11]. The photovoltaic performance results indicated that devices based on crown ether-end-capped PM6E7 exhibited better stability and PCE than the reference PM6-based cells. The improved device performance can be attributed to appropriate molecular weight, better morphology, fewer end traps, higher crystallinity, and balanced mobility. These results demonstrated that end-capping groups of the conjugated polymers can minimize the undesired molecular defects, which is helpful in suppressing charge

Citation: Liu T, Li X, Liu J, Li Y, Gao X, Huang H, Huang R, Zhang Q, Wang M, He H, Ma CQ. H/F/Cl substituted naphthalenyl end-capped PM6 for high-performance organic solar cells. *Sci China Chem*, 2026, 69: 362–370. https://doi.org/10.1007/s11426-025-2766-3

recombination and ensuring effective exciton dissociation and charge extraction. Except for the examples mentioned above, limited research has been reported in the literature. The reasons and mechanisms underlying the effects of end-capping on polymer device performance have not been fully studied. Summarizing the principles governing the relationship between end-capping and performance is of great significance for improving the photovoltaic performance of polymers.

In this study, naphthyl and F-/Cl-substituted naphthyl end-capped polymers named PM6-H, PM6-F, and PM6-Cl were synthesized and characterized. End-capping of the conjugated polymers was verified using matrix-assisted laser desorption/ ionization time-of-flight mass spectra (MALDI-TOF-MS). Solar cells based on PM6-H:L8-BO, PM6-F:L8-BO, and PM6-Cl:L8-BO were fabricated, and the corresponding device characteristics were carefully investigated. The intense interaction between PM6-Cl and L8-BO promoted the optimal distribution of the active layer, enhanced charge transport, and achieved a finer film morphology. By systematically optimizing film formation processes, devices based on PM6-Cl:L8-BO achieved an optimal PCE of up to 18.07%, one of the high-performance devices based on end-capped PM6, demonstrating that end-capping could further tune the donor-acceptor aggregation, charge transport, vertical phase distribution, and morphology of the active layer, and thus optimize device performance.

2 Experimental

2.1 Synthesis of PM6-X (X = H, F, Cl)

The trimethylstannyl monomer ($Me_3SnDSnMe_3$) (200 mg, 0.213 mmol), the bromo-substituted monomer (BrABr) (190 mg, 0.248 mmol), and 60 mL dry toluene were added to a dry 100 mL Schlenk bottle. The mixture was purged with nitrogen, and then Pd $(PPh_3)_4$ (3.1 mg, 2.68 μmol) was added. The resulting mixture was purged with nitrogen again for 30 min and then stirred at 90 °C for 22 h. After cooling to room temperature, tin monomer ($Me_3SnDSnMe_3$) (66.7 mg, 0.071 mmol) was added to the mixture, and then stirring was continued at 90 °C for 4 h. Small portion of Pd_2dba_3 (3.1 mg, 3.38 μmol) and $P(o\text{-}tol)_3$ (6.2 mg, 20.31 μmol) with 2-bromonaphthalene (29.4 mg, 0.142 mmol) was then added to the reaction mixture for the final end-caping. The reaction was then heated to 90 °C for 24 h and then raised to 110 °C to continue the reaction for 24 h. Finally, the reaction mixture was cooled to room temperature and the product was precipitated using methanol. Collect the black solid by filtration, dissolve the polymer in chloroform solvent, and use chloroform as an eluent to pass through a coarse silica gel flash column. The polymer solution was rotary evaporated to remove the solvent and then dropped into methanol. The target copolymer was obtained by filtration and dried in a vacuum oven at 40 °C overnight to obtain a purple-black solid with metallic luster (261 mg, 79%).

The fluoro- and chloro-naphthyl end-capped PM6 were synthesized by a similar protocol, with 6-fluoro-2-bromonaphthanlene and 6-chloro-2-bromonaphthanlene replacing 2-bromonaphthalene as the end-capping reagent. PM6 without end-capping was also synthesized as a reference (PM6S). More information on the synthesis and purification of PM6-F, PM6-Cl and PM6S can be found in the Supporting Information.

2.2 Device fabrication

The ITO substrates underwent a sequential cleaning process, consisting of 20-min treatments in detergent, de-ionized water, acetone, and ethanol, respectively. The cleaned ITO substrates were further subjected to an oxygen plasma treatment for 30 min. The PEDOT:PSS film was spin-coated on the substrate at 3500 r/min, annealed at 150 °C for 15 min in an air environment, and then transferred to the glove box. Subsequently, the mixture solution was spin-coated on the PEDOT:PSS layer at 3500 r/min for 30 s to form an active layer of approximately 100 nm, in which PM6-H:L8-BO, PM6-F:L8-BO, PM6-Cl:L8-BO, PM6S:L8-BO, PM6B:L8-BO (D:A = 1:1.2, 10 mg mL^{-1} TCB) were dissolved in chloroform at the total concentration of 16.5 mg mL^{-1} and stirred at 60 °C for 4 h. After spin coating, all films were annealed at 100 °C for 10 min. Subsequently, PDINN layers with a thickness of approximately 10 nm were spin-coated onto the active layers. Finally, 100 nm thick Ag layers were thermally evaporated through shadow masks to complete the fabrication of the devices. The device contact area was 0.04 cm^2.

3 Results and discussion

3.1 Molecular structure and characterization

Fluoronaphthalene and chloronaphthalene were commonly used in the OSCs fabrication. They could effectively adjust the morphology of the active layer, improve electron mobility, enhance electron transportation, and thus improve device performance. The purpose of end-capping of polymers was to improve the polymer-based OSC performance. Therefore, we chose three naphthalene capping agents with different electron-withdrawing characteristics. The chemical structure of end-capped PM6 is shown in Figure 1a, where H-, F-, and Cl-substituted naphthalenyl groups with different electron-withdrawing properties were attached to the chain end of the polymers, which are named PM6-H, PM6-F, and PM6-Cl, respectively. To better understand the end-capping effect on the properties of the resulting polymers, we investigated electrostatic potential surfaces (ESP) and dipole moments of three model compounds based on benzo[1,2-b:4,5-b′]dithiophene (BDT) coupled to the substituted naphthalene, named BDTNH, BDTNF, and BDTNCl, respectively. As seen in Figure 1a, these three terminal groups exhibit similar negative charge distribution over the conjugation chain, with the Cl-terminated BDTNCl showing a slightly higher electron density. This can be attributed to the fact that the Cl atom is more electron-rich than the F atom. In contrast, the electron acceptor, L8-BO, had a predominantly positive charge distribution throughout the main chain [14]. Therefore, end-capped polymers should tend to interact more strongly with L8-BO due to robust intermolecular interactions [14]. Furthermore, we calculated the dipole moments of the end-capping groups, with values of 0.47 D for BDTNH, 1.03 D for BDTNF, and 1.94 D for BDTNCl. It should be noted that BDTNCl had a larger dipole moment than BDTNF, as the larger Cl atom induces stronger conjugation with the naphthalene ring compared to the F atom. The larger dipole moments could induce higher dielectric constants and stronger intermolecular interactions, which could reduce exciton binding energy and charge recombination losses [15,16]. In addition, the increased dipole moment of BDTNCl should enhance intermolecular interaction between PM6-Cl and L8-BO, which might facilitate the formation of a favorable morphology for stacking, thus promoting charge collection and transport [17,18].

The polymers were end-capped by adding the naphthalenyl reagent to the reaction mixture at the final step of the synthesis (Table 1). Detailed experimental procedures are provided in the Supporting Information online. The molecular weight of the resulting polymers was tested with high-temperature GPC, and number-average molecular weights (M_n) of PM6-H, PM6-F, and

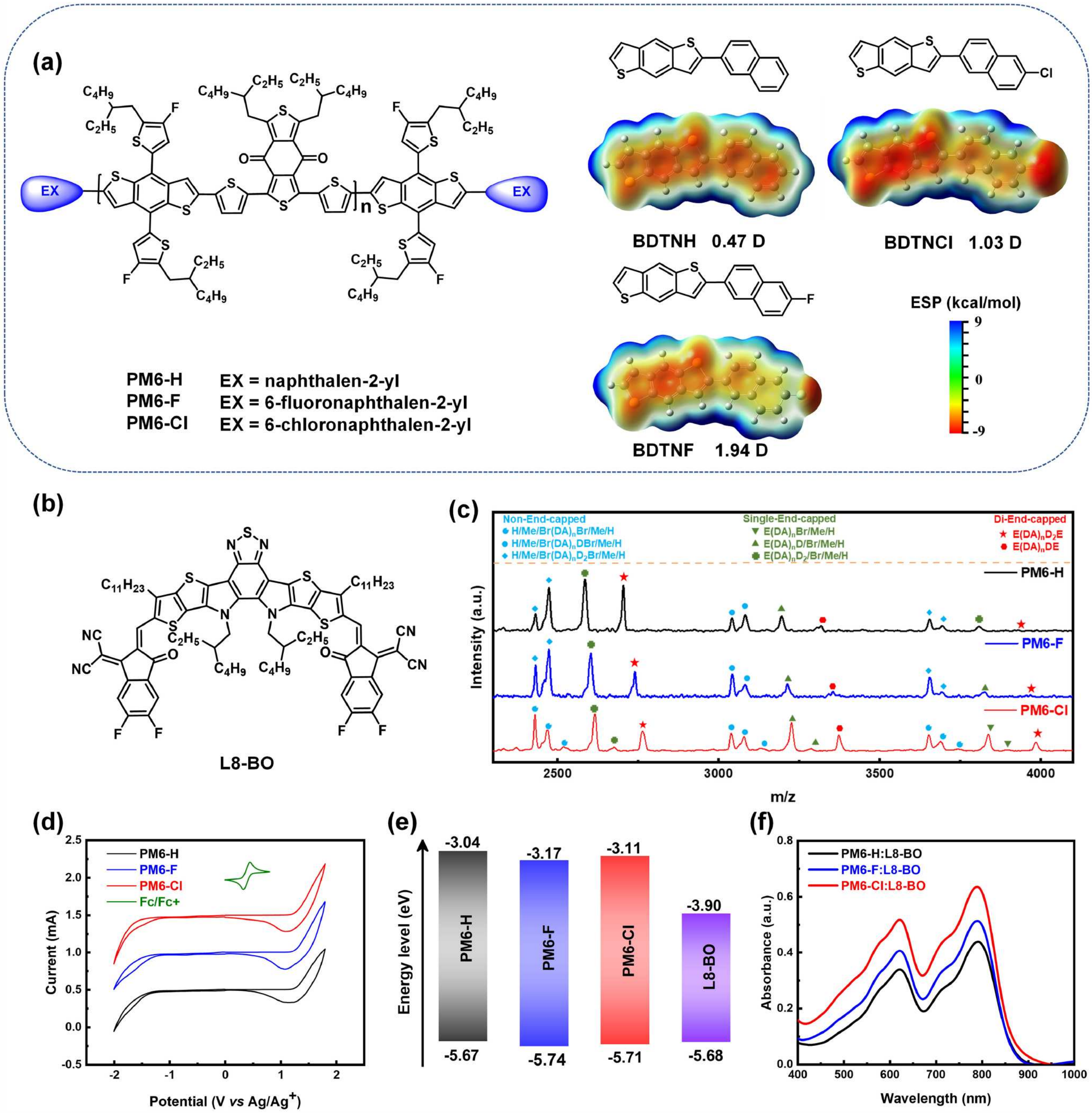

Figure 1 (Color online) (a) Molecular structures of naphthene-end-capped PM6 and ESP distributions of the terminal groups. (b) ESP distributions of L8-BO. (c) MALDI-TOF-MS spectra of PM6-H, PM6-F and PM6-Cl, and the corresponding structures of some main peaks. (d) Cyclic voltammetry curves. (e) Energy level diagrams of end-capped polymers. (f) Normalized UV-Vis absorption spectra of blend films in chloroform solution.

Table 1 End-capping yields and molecular weights of three polymers

Polymer	End-capping reagent	End-capping yield (%)	M_n (kg mol^{-1})	M_w (kg mol^{-1})	PDI	λ_{max} (nm)	E_g^{opt} (ev)
PM6-H	2-bronaphthalene	67.0	12.6	40.3	3.19	668	1.80
PM6-F	2-bromo-6-fluoronaphthalene	64.4	11.4	38.8	3.39	693	1.79
PM6-Cl	2-bromo-6-chloronaphthalene	64.3	12.0	46.4	3.86	695	1.78

PM6-Cl were determined to be 12.6, 11.4, and 12.0 kg mol^{-1}, with polydispersity indices (PDI) of 3.19, 3.39, and 3.86, respectively (Figure S1, Supporting Information online). All three polymers have similar molecular weights of around 12.0 kg mol^{-1}, indicating that the final end-capping step doesn't influence the polymerization process too much. Additionally, MALDI-TOF-MS of these three polymers was tested, and the results are shown in Figure 1c. In addition to the mono- and double-end-capped molecules (marked as green and red symbols), un-end-capped molecules were also tested (marked as blue symbols), indicating that end-capping was not fully complete and further optimization of the end-capping reaction is still needed. The end-capping yields of around 65% were calculated for all three of these polymers, validating a reasonable end-capping efficiency. As shown later, the resulting polymer demonstrates the end-capping effect on the photovoltaic performance. In general, a high end-capping ratio of the final polymer would be beneficial in achieving high-performance polymers. Further optimization of the end-capping reaction conditions is of great importance for the synthesis of functional conjugated polymers.

The influence of end-groups on the energy levels of conjugated polymer materials was investigated by using cyclic voltammetry (CV), and the energy level distributions are shown in Figure 1d, e. The highest occupied molecular orbital (HOMO) energy levels of PM6-H, PM6-F, and PM6-Cl were estimated to be −5.67, −5.74, and −5.71 eV, while their lowest unoccupied molecular orbital (LUMO) energy levels were −3.04, −3.17, and −3.11 eV, respectively. These results demonstrated that the PM6-F and PM6-Cl with halogen atom substitutions exhibit lower HOMO and LUMO energy levels when compared to PM6-H, attributed to the electron-withdrawing ability of different atoms, following the order F > Cl > H [19]. The lower HOMO values of PM6-F and PM6-Cl would result in higher V_{OC} in the final OSC devices [20,21]. Subsequently, the light absorption properties of PM6 capped with different naphthalene derivatives in chloroform solution and films and their blends with L8-BO in chloroform solution were also studied. The normalized UV-Vis absorption spectra of the hybrid films are shown in Figure 1f, where two distinct absorption peaks corresponding to end-capped PM6 and acceptor L8-BO could be observed. The absorption band over 700 to 850 nm originates from the L8-BO, while the absorption band over 500 to 700 nm belongs to the absorption of the polymer donor. PM6-Cl had a broader absorption peak, possibly due to better complementation with L8-BO. Among them, the PM6-Cl:L8-BO film exhibited the highest absorption intensity and most substantial shoulder peak, which would enhance the J_{SC} of OSCs [22]. Meanwhile, Figure S2 depicts the normalized UV-vis absorption spectra of PM6-H, PM6-F, and PM6-Cl films in chloroform solution and thin films. The aggregation strength of the polymer could be evaluated according to the intensity ratio between the $\lambda_{0\text{-}0}$ peak and the $\lambda_{0\text{-}1}$ peak ($I_{0\text{-}0}/I_{0\text{-}1}$) [15]. PM6-Cl had a higher $I_{0\text{-}0}/I_{0\text{-}1}$ ratio with a slightly red-shifted (0-0) absorption band both in solution and thin solid film, indicating that PM6-Cl had a more intensive aggregation behavior. Experimental data indicate that the end-capping group could modulate the aggregation state of these polymer donors.

3.2 Thin film topography analysis

The morphology of the active layer played a crucial role in understanding the photovoltaic performance and working mechanisms [23]. Atomic force microscopy (AFM) was utilized to investigate the microstructure of pristine end-capped polymer and the blend film of the best OSCs. Figure 2a–i depicts the height and phase images of the blend films, and the measured root mean square roughness (RMS) of the films is listed in Figure 2j. For comparison, the AFM images of the pristine polymer films are shown in Figure S3. All these pristine polymer films showed smooth surfaces with RMS of 0.93, 0.88, and 0.83 nm for PM6-H, PM6-F, and PM6-Cl, respectively. After blending with L8-BO acceptors, the PM6-H:L8-BO, PM6-F:L8-BO, and PM6-Cl:L8-BO films exhibited RMS of 1.13, 1.05, and 0.88 nm, respectively. Slightly increased surface roughness of the PM6-H and PM6-F-based films could be ascribed to the increased crystallinity of L8-BO in the blend film. Whereas the PM6-Cl-based blend film remained relatively smooth and exhibited a well-refined continuous interpenetrating network, indicating that PM6-Cl can suppress excessive penetration of L8-BO within the blend film, thereby reducing the over-crystallization of L8-BO, resulting in balanced donor-acceptor phase regions [24,25]. Additionally, the phase images revealed fibrous nanostructure in the polymer and blended film, suggesting the formation of interpenetrated nanostructures [26]. The experimental data suggested that the end-capping groups could further modulate the morphology of blend films.

To gain a deeper insight into the molecular orientation and stacking behaviors, grazing incidence wide-angle X-ray scattering (GIWAXS) was employed to measure the pristine and blended polymer films of the best OSCs. As depicted in Figure S4, weak diffraction peaks were observed in pristine polymer films. Among them, PM6-Cl had a slightly higher crystallinity of 69.78 and 18.80 nm in the in-plane (IP) and out-of-plane directions (OOP), respectively. It also had a tight π-π stacking distance of 3.65 Å in the OOP direction. Two-dimensional GIWAXS patterns of blend films are shown in Figure 2g–i, with specific parameters listed in Table S1 (Supporting Information online). All blend films exhibited a weak π-π stacking peak (010) crystal plane in the OOP direction and a layered stacking peak (100) crystal plane in the IP direction, indicating a preference for “face-on” stacking in the vertical direction, which is beneficial for charge transportation [27,28]. In the OOP direction, the diffraction values q_z for PM6-H:L8-BO, PM6-F:L8-BO, and PM6-Cl:L8-BO films were measured as 1.72, 1.73, and 1.74 $\mathrm{Å}^{-1}$, with π-π stacking distances of 3.65, 3.63, and 3.61 Å, and coherent crystal lengths (CCL) of 22.13, 22.78, and 23.32 Å, respectively. Similarly, in the IP direction, the diffraction values q_{xy} for PM6-H:L8-BO, PM6-F:L8-BO, and PM6-Cl:L8-BO films were calculated to be 0.039, 0.311, and 0.312 $\mathrm{Å}^{-1}$, with layered stacking distances of 20.32, 20.19, and 20.12 Å, and CCL of 74.97, 94.80, and 104.22 nm, respectively. Clearly, end-capping of the conjugated polymer had a certain influence on molecular arrangement. The PM6-H:L8-BO exhibited the lowest CCL value, indicating the smallest crystal size and the lowest phase purity. Conversely, PM6-Cl:L8-BO films displayed the strongest diffraction signals and intensities, with clear layered stacking peaks, indicating the tightest π-π stacking. The smallest π-π stacking distance also suggested the strongest intermolecular interactions between PM6-Cl and L8-BO [29]. PM6-Cl:L8-BO films exhibited optimal stacking order and moderate phase-separated morphology. The alteration of end-group atoms will further regulate molecular stacking and morphology of the active layer, thereby enhancing device performance.

3.3 Device physics

To further investigate the effects of different end groups on the performance of polymer-based devices, we fabricated bulk heterojunction organic solar cells using a conventional ITO/PEDOT:PSS/Active layer/PDINN/Ag structure. Detailed device fabrication procedures are provided in the supplementary information. By adjusting the donor:acceptor (D:A) blend ratio of the active layer, additive, annealing temperature, and film thickness, we explored the optimal device conditions. Table 2 lists the photovoltaic performance parameters of the optimized devices, and Figure 3b shows the corresponding *J-V* curves of the polymer-based OSCs. For comparison, devices based on commercially available PM6 (PM6B) and non-end-capped PM6 synthesized in our lab according to the same synthesis procedure (PM6S) were also fabricated and tested. As seen in Table 2, substituting terminal groups of the conjugated polymer could significantly alter device performance. Among them, the device based on PM6-Cl:L8-BO showed the best photovoltaic performance, with a PCE of 18.07%, which is close to the PCE of 18.35% of the device based on PM6B:L8-BO. In addition, the J_{SC} of the device based on PM6-Cl:L8-BO was slightly higher than that of the device based on PM6B:L8-BO. The significant enhancement in PCE is attributed to increased J_{SC} (26.07 mA cm^{-2}) and FF (77.57%), which could be due to enhanced charge carrier mobility

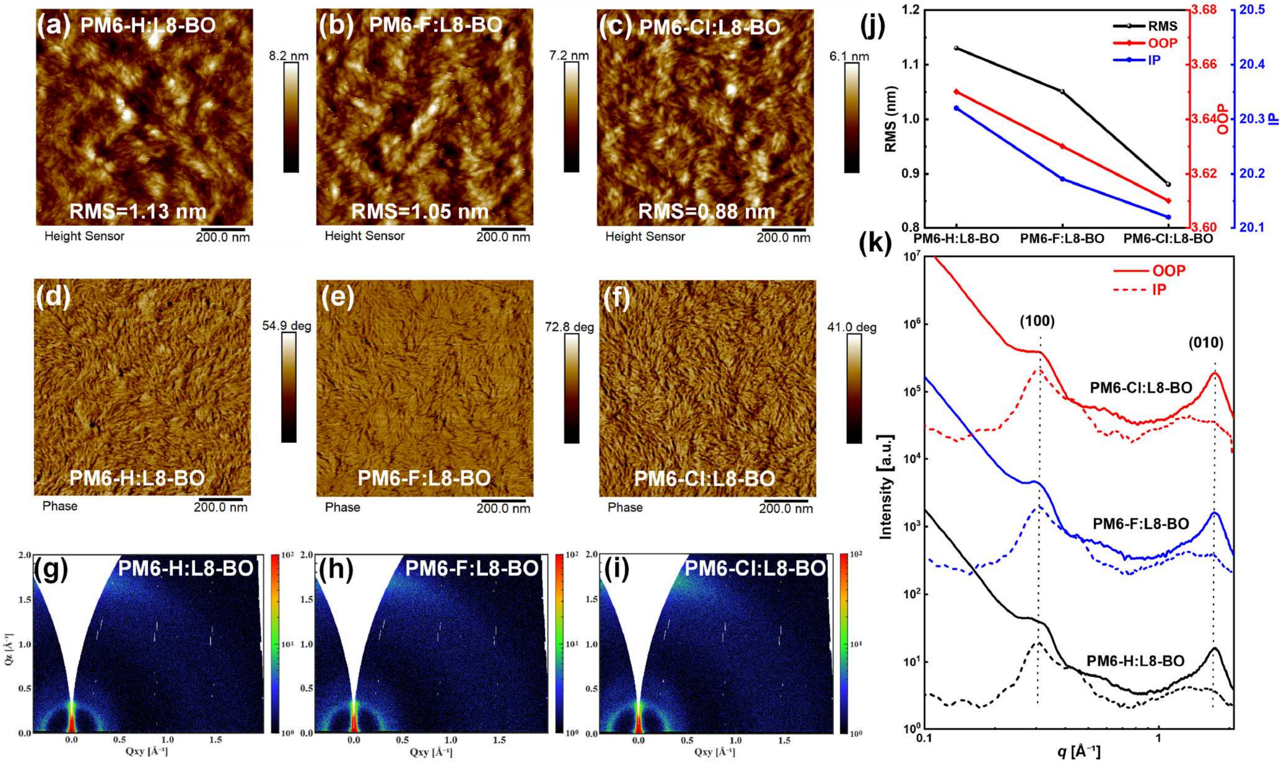

Figure 2 (Color online) AFM height (a–c) and phase (d–f) images of (a) PM6-H:L8-BO, (b) PM6-F:L8-BO, and (c) PM6-Cl:L8-BO films; 2D-GIWAXS profile of (g) PM6-H:L8-BO, (h) PM6-F:L8-BO, and (i) PM6-Cl:L8-BO films. (j) Roughness (RMS), π-π stacking and lamellar stacking distance of various films; (k) OOP and IP wire cutting profiles of PM6-H:L8-BO, PM6-F:L8-BO, and PM6-Cl:L8-BO films.

Table 2 Photovoltaic performance of OSCs based on different active layers under AM 1.5 G 100 mW/cm^2 light

Active layer	V_{OC} (V)	J_{SC} (mA cm^{-2})	FF (%)	PCE (%)$^{a)}$
PM6-H:L8-BO	0.890 (0.888±0.002)	25.24 (24.71±0.38)	75.36 (75.35±0.06)	16.87 (16.53±0.29)
PM6-F:L8-BO	0.890 (0.888±0.005)	25.83 (25.18±0.41)	76.55 (76.36±0.66)	17.60 (17.08±0.33)
PM6-Cl:L8-BO	0.894 (0.891±0.002)	26.07 (25.95±0.18)	77.57 (76.76±0.84)	18.07 (17.75±0.34)
PM6B:L8-BO	0.903 (0.906±0.004)	26.02 (25.40±0.54)	78.12 (78.15±0.61)	18.35 (17.99±0.37)
PM6S:L8-BO	0.860 (0.860±0.004)	24.08 (23.70±0.27)	70.84 (70.72±0.97)	14.67 (14.41±0.29)

a) In parentheses are based on the average of more than ten individual devices.

and charge transfer efficiency. The authenticity of J_{SC} in the binary system was verified through external quantum efficiency (EQE) testing, as shown in Figure 3c. The PM6-Cl:L8-BO device showed a high spectral response in the wavelength region of 350–800 nm, contributing to a higher J_{SC}. The calculated current densities from EQE (J_{EQE}) spectra were 24.07, 24.77, and 25.31 mA cm^{-2} for PM6-H, PM6-F, and PM6-Cl-based OSCs, respectively. The J_{EQE} matched well with the values obtained from J-V measurements. In contrast, all devices exhibited relatively high V_{OC}s, indicating that end-capping of the conjugated polymer doesn't influence the Fermi level splitting within the films under light illumination. The statistical histograms of PCE, summarized from 10 devices, are shown in Figure 3i. As shown in Table 2, the end-capped PM6 exhibited higher PCE than PM6S, while the PM6S-based OSCs exhibited the worst photovoltaic performance among these polymers. It should be noted that there was plenty of space for us to improve the synthesis of conjugated polymers. This was easily understood that residual end groups (–Sn, –Br) could trap excitons and charge carriers, which was also studied in our previous articles [11,30]. It should be noted that the synthesized PM6 derivative showed poorer performance than commercially available PM6B, indicating that further optimization of the polymerization reaction is still needed.

Figure 3i displays the electron impedance spectra (EIS) of different PM6-based cells, revealing two asymmetric semicircles in all EIS spectra. The PM6-Cl:L8-BO-based device exhibited the smallest impedance compared to the other two polymers, indicating the lowest resistance and best carrier transport of the cells [31–33]. This was because chloronaphthalene has stronger van der Waals interactions with the acceptor end groups than fluoronaphthalene. Knowing that chloronaphthalene is widely used solvent additive for fine-tuning the nanomorphology of the polymer blend owing to the electronic coupling between acceptor molecules [34], together with the that the terminal BDTNCl unit has a stronger interaction with L8-BO acceptor molecules than BDTNF (*vide supra*), the lower resistance of PM6-Cl based cells can be attributed to the reduce the intermolecular π-π stacking distance and enhance the carrier transport capability within the film.

The charge carrier transport properties were measured using the steady-state space charge limited current (SCLC) method [35,36]. The hole-only (ITO/PEDOT:PSS/Active layer/MoO$_3$/Ag) and electron-only (ITO/ZnO/Active layer/PDINN/Ag) devices were fabricated and tested. Both the hole mobility (μ_h) and electron mobility (μ_e) of the corresponding devices were calculated and summarized

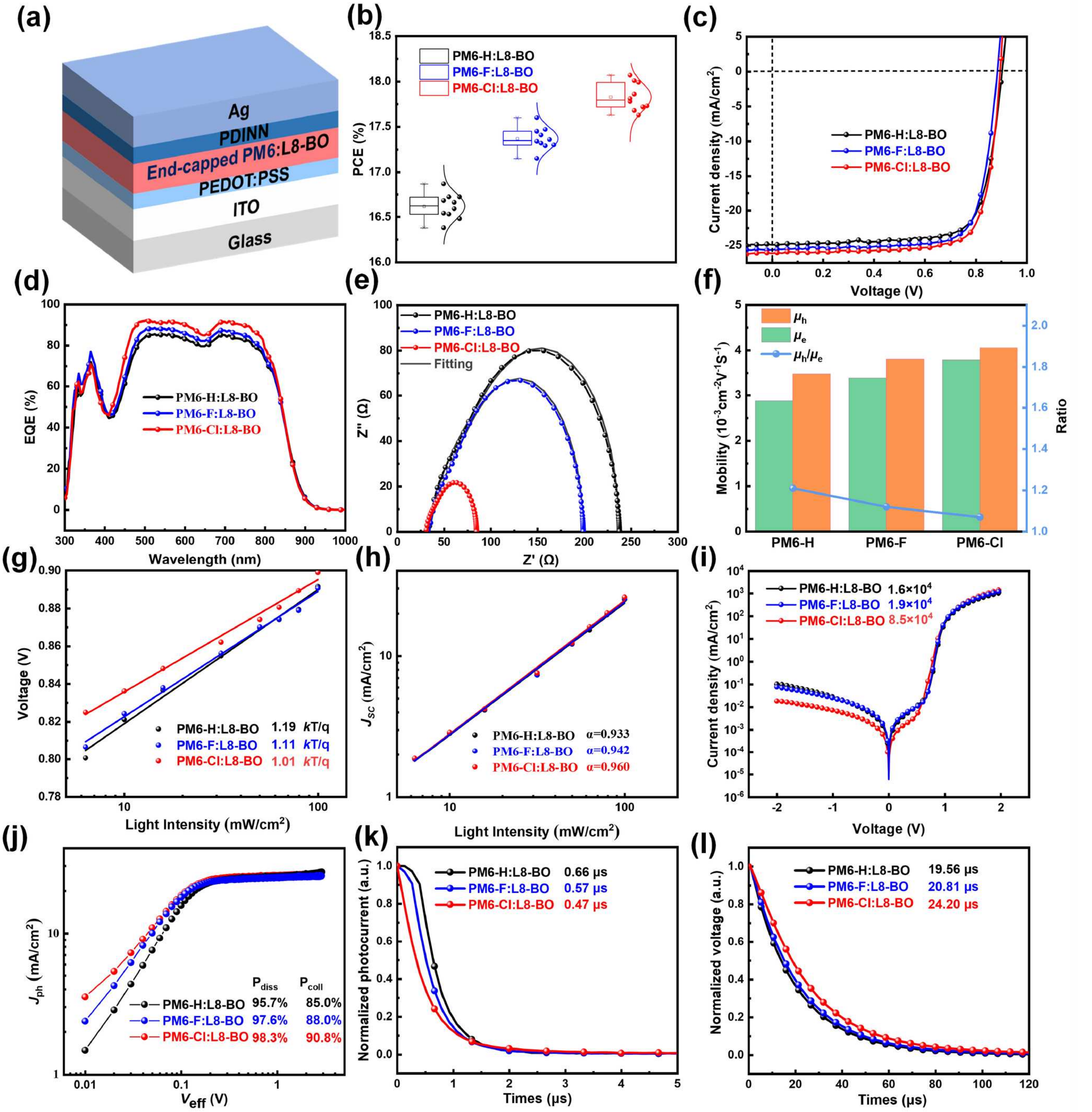

Figure 3 (Color online) (a) The structural diagram of conventional organic solar cells; (b) efficiency statistical histograms of the cells based on different polymers; (c) *J-V* curves and (d) EQE of the cells; (e) electronic impedance spectra (EIS) of the cells; (f) the measured electron (μ_e) and hole (μ_h) mobilities and the μ_e/μ_h ratios of polymer:L8-BO cells; light intensity dependence of V_{OC} (g) and J_{SC} (h) of the cells; dark *J-V* curves (i), J_{ph}-V_{eff} characteristics (j), transient photo current (TPC), curves (k) and transient photo voltage (TPV) curves (l) of cells based on different polymers.

in Figure 2f, Figure S5 and Table S2. Experimental data indicated that the μ_h/μ_e values for PM6-H:L8-BO, PM6-F:L8-BO, and PM6-Cl:L8-BO films were $3.48\times10^{-3}/2.88\times10^{-3}$, $3.81\times10^{-3}/3.38\times10^{-3}$, and $4.06\times10^{-3}/3.79\times10^{-3}$ cm^2 V^{-1} s^{-1}, respectively. Their corresponding μ_h/μ_e ratios were 1.21, 1.12, and 1.07, respectively. PM6-Cl exhibited not only the highest carrier mobility but also the most balanced hole/electron mobility ratio. Films with optimal stacking order facilitate charge transport between donor and acceptor materials, balancing exciton dissociation and enhancing charge collection. Different end-group polymers regulated carrier transport by affecting the morphology of the active layer. PM6-Cl-based films had the best morphology, so the device based on PM6-Cl:L8-BO achieved the most efficient charge transport, ultimately achieving the best FF value (77.57%) and the highest J_{SC} value (26.07 mA cm^{-2}).

To gain deeper insights into the effect of end groups on the charge recombination dynamics in OSCs, incident light intensity (P_{light})-dependent *J-V* characteristics of the cells were measured and analyzed. Figure 3g, h depicts the relationship between measured V_{OC} and J_{SC} with P_{light}. A linear correlation of V_{OC} with logarithmic P_{light} was found, and the slope of the line gives the ideality (n) of the cells according to the equation: $V_{OC} \propto nkT/q\ln(P_{light})$, where n, K, T, and q represent constants, the Boltzmann constant, temperature in Kelvin, and elementary charge, respectively. The n values for PM6-H:L8-BO, PM6-F:L8-BO, and PM6-Cl:L8-BO-based OSCs were calculated to be 1.19, 1.11, and 1.01, respectively. The n of the

PM6-Cl:L8-BO active layer was the smallest, indicating the most effective suppression of trap-assisted and single-molecule recombination [37]. This also explains the best J_{SC} and PCE of the PM6-Cl-based cells. Similarly, a linear relationship between J_{SC} and $\ln(P_{light})$ was found, and the exponent factor α for the equation $J_{SC} \propto P_{light}{}^{\alpha}$ was measured to be 0.933, 0.942, and 0.960 for PM6-H:L8-BO, PM6-F:L8-BO, and PM6-Cl:L8-BO-based OSCs, respectively. The α of PM6-Cl:L8-BO-based cell approaches 1, indicating a higher degree of suppression of bimolecular recombination [38]. Again, the light intensity dependent measurement suggested that the ordered molecular packing and shortened π-π stacking optimizes the charge collection process of OSCs, and the PM6-Cl:L8-BO device was more effective in suppressing bimolecular recombination and exhibited the highest FF [39].

To investigate the influence of exciton dissociation within the polymer active layer, the relationship between the photocurrent density (J_{ph}) and effective voltage (V_{eff}) of the optimized OSCs was also studied. The equations $J_{ph} = J_L - J_D$ (where J_L and J_D represent the current densities under illumination and dark conditions, respectively) and $V_{eff} = V_0 - V_{bias}$ (where V_0 and V_{bias} represent the voltage at $J_{ph} = 0$ and the applied bias voltage, respectively) were used to calculate parameters [40]. J_{sat} is mainly determined by the number of photons collected by the active layer, which represents the saturation current density when V_{eff} = 2 V. The current density at the short-circuit and the maximum power output conditions are J_{ph}^{*} and $J_{ph}^{\&}$, respectively. Under short-circuit conditions, the exciton dissociation efficiency (P_{diss}) could be calculated by using the formula $P_{diss}= J_{ph}^{*}/J_{ph}^{\&}$, and the charge collection efficiency (P_{coll}) could be calculated by using the formula $P_{coll} = J_{ph}^{*}/J_{ph}^{\&}$ [41]. Therefore, the P_{diss}/P_{coll} values for devices based on PM6-H:L8-BO, PM6-F:L8-BO, and PM6-Cl:L8-BO were measured to be 96%/85%, 98%/88%, and 98%/91%, respectively. Interestingly, all OSCs exhibited P_{diss} exceeding 95%, indicating high exciton dissociation efficiency in all devices. Devices based on PM6-Cl:L8-BO showed the fastest exciton dissociation rates and highest charge collection efficiency compared to those based on PM6-F:L8-BO and PM6-Cl:L8-BO, in good consistent with the J_{SC} results [41,42]. These findings revealed the carrier dynamics and recombination processes in PM6-H, PM6-F, and PM6-Cl-based devices, contributing to a better understanding of their photovoltaic performance.

In addition, the dark *J-V* characteristic curves of the OSCs were also investigated. As shown in Figure 3d, the rectification ratios for devices based on PM6-H:L8-BO, PM6-F:L8-BO, and PM6-Cl:L8-BO were calculated to be 1.6×10^4, 1.9×10^4, and 8.5×10^4, respectively. Notably, the PM6-Cl:L8-BO-based device exhibited the highest rectification ratio. This indicated the most effective charge selectivity in this system, which would benefit the improvement of the device FF.

To quantitatively analyze the charge extraction and recombination modes of the three polymer devices, transient photocurrent (TPC) and transient photovoltage (TPV) measurements were conducted [43]. The charge extraction time was calculated from the TPC decay curve, as shown in Figure 3k. The charge extraction times for devices based on PM6-H:L8-BO, PM6-F:L8-BO, and PM6-Cl:L8-BO were 0.7, 0.6, and 0.5 μs, respectively. This indicated that devices based on the PM6-Cl:L8-BO system could effectively promote the charge extraction process, significantly enhancing the FF of OSCs. Moreover, the shortened charge extraction time was consistent with the higher charge collection efficiency (P_{coll} = 91%) observed in PM6-Cl:L8-BO-based devices. Carrier lifetimes were calculated by fitting the TPV curves, as shown in Figure 3i. According to the fitting data, the carrier lifetime for PM6-Cl:L8-BO was 24.2 μs, higher than PM6-H:L8-BO (19.6 μs) and PM6-F:L8-BO (20.8 μs) devices. The higher carrier lifetime in PM6-Cl:L8-BO indicated effective suppression of carrier recombination, promoting the enhancement of J_{SC} [44]. Therefore, the synergistic effect of faster charge extraction and less free carrier recombination in PM6-Cl:L8-BO-based devices results in higher J_{SC} and FF [45].

3.4 Phase separation of the active layer and its mechanism analysis

Good compatibility between the polymer donor and acceptor was crucial for forming well-defined morphologies in blends. To investigate the compatibility between the polymer donor and acceptor, the contact angles of pristine and blend films based on water and diiodomethane were measured. The corresponding surface free energy (γ) values were calculated. The measured contact angles of PM6-H, PM6-F, PM6-Cl, and L8-BO were 103.99°, 106.09°, 107.71°, and 94.84°, respectively. These values were all higher than 90°, indicating strong hydrophobicity of the organic solar cell materials. The surface energies of PM6-H, PM6-F, PM6-Cl, and L8-BO pristine films were measured to be 24.99, 26.74, and 28.18 mN/m, respectively. The contact angles of PM6-H:L8-BO, PM6-F:L8-BO, and PM6-Cl:L8-BO were 106.09°, 105.52°, and 106.81°, respectively (Figure S6), indicating that the prepared bulk heterojunction devices had a higher enrichment of donor material near the side of the hole transport layer. For cells with a normal structure, holes need to be transported through the hole transport layer to the anode. Therefore, the more enrichment of the donor material near the PEDOT:PSS side, the more suitable for hole transportation.

To better illustrate their compatibility, the Flory-Huggins interaction parameter (χ) for the donor-acceptor was calculated using the formula:

$$\chi_{\text{donor-acceptor}} = k\left(\gamma_{\text{donor}}^{\frac{1}{2}} - \gamma_{\text{acceptor}}^{\frac{1}{2}}\right)^2 \tag{1}$$

where γ_{donor} and $\gamma_{acceptor}$ are the surface energies of the donor and acceptor, respectively, and k was a constant (Table S3) [46,47]. Among them, the interaction parameter χ calculated from the surface free energies of PM6-Cl and L8-BO was the smallest (χ = 1.02 K), indicating the best compatibility between the polymer PM6-Cl and the acceptor L8-BO, facilitating the formation of a uniform and stable blend morphology [29,48,49].

The vertical distribution of the polymer donor and acceptor in thin films was measured using time-of-flight secondary ion mass spectrometry (TOF-SIMS). For simplicity and clarity, the device structure was chosen as ITO/PEDOT:PSS/Active layer. In addition, from the molecular structures, the characteristic elements of the end-capped PM6 and L8-BO were determined to be S and CN, respectively. As shown in Figure S7, the active layer was identified to be within the range of 50 to 150 s by tracking these characteristic elements. It is worth noting that the InO^- and InO_2^- signals were measured at almost the same time (around 110 s) for these three samples (Figure S7), indicating that there is no significant layer thickness difference for these films. It was observed that the intensity of the CN element next to the PEDOT:PSS was lower, indicating a lower donor concentration at the PEDOT:PSS interface. In other words, a higher donor ratio at the bottom of the photoactive layer. To give a deep insight into the vertical distribution of the donor and acceptor components, the CN/S ratios of these films were measured, both of which give a hint of the acceptor-to-donor ratio since CN comes only from the acceptor molecules and S comes mostly from the donor molecules. To minimize the slight variation of layer thickness, the sputtering time was normalized to the beginning of

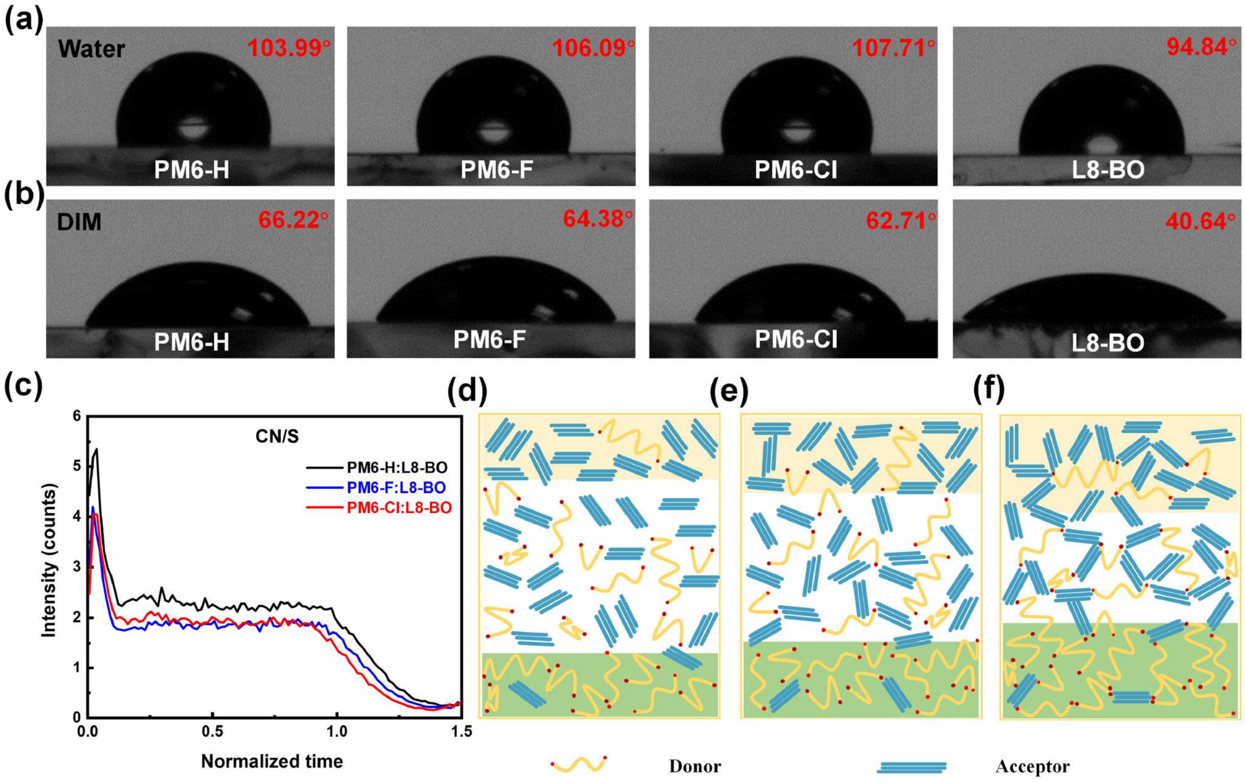

Figure 4 (Color online) Contact angles measurement of (a) water and (b) diiodomethane on PM6-H, PM6-F, PM6-Cl, and L8-BO film. (c) Ratios of CN/S intensity in blend film measured by TOF-SIMS. Mechanism diagram of (d) PM6-H:L8-BO, (e) PM6-F:L8-BO, and (f) PM6-Cl:L8-BO films (the yellow and green shaded parts represent acceptor-rich and donor-rich parts, respectively).

the InO_2^- signal, and Figure 4c presents the results. As seen here, PM6-Cl showed the lowest CN/S ratio near PEDOT:PSS, while PM6-H showed the highest, indicating a slightly higher donor ratio at the PEDOT:PSS surface for the PM6-Cl-based films. Generally, a higher percentage of donors near the PEDOT:PSS layer could benefit from high PCE. The gradient distribution suggested that the end-capping could inhibit excessive diffusion between the donor and acceptor, thereby constructing a well-defined vertical phase distribution. Therefore, devices based on PM6-Cl:L8-BO facilitated easier charge transport and collection, consistent with higher FF and performance of the devices [50]. Figure 4d–f describes the interactions, phase separation, and vertical phase distribution of the donor-acceptor in different active layers. In the PM6-H-based active layer, the donor-acceptor interaction was the weakest, with the largest phase separation and poorest vertical phase distribution [51]. In contrast, PM6-Cl exhibited the strongest interactions with L8-BO, the smallest phase separation, the best film distribution, and the most ordered distribution of donor and acceptor, leading to the highest performance of devices based on PM6-Cl:L8-BO [52]. Experimental data suggested that changes in end-group atoms could further regulate the active layer's phase separation and vertical phase distribution, which could be attributed to different end-capping groups having different dipole moments and interaction with the L8-BO.

4 Conclusions

In summary, we systematically investigated the mechanism by which different end-group substitutions affect the performance of end-capped PM6 devices. The strong electron-withdrawing ability of the end-capping reagents resulted in lower HOMO energy levels for all three polymers, corresponding to higher voltages in the polymer devices. The larger dipole moment of BDTNCl increased the interaction between chloronaphthyl-end-capped PM6 and the acceptor, leading to a more ordered structure in the active layer and a shortened π-π stacking distance, thereby enhancing charge transport capability. Devices based on PM6-Cl:L8-BO exhibited the best blend morphology, most balanced charge mobility, highest carrier lifetime, lowest charge recombination, and most suitable phase separation among these films. Consequently, the PM6-Cl-based OSCs achieved an efficient PCE of 18.07%, with a V_{OC} of 0.894 V, J_{SC} of 26.07 mA cm^{-2}, and FF of 77.57%. This work not only demonstrated the effective modulation of device performance through end-capping strategies but also highlighted the potential for precise control over material energy levels, film morphology, crystallinity, and phase separation using appropriate end-capping groups.

Conflict of interest

The authors declare no conflict of interest.

Acknowledgement

This work was supported by the National Natural Science Foundation of China (NSFC) (52203249), the Young Innovation Leading Talents of Suzhou Innovation and Entrepreneurship Leading Talents Program (ZXL2022462) and the Suzhou Institute of Nano-Tech and Nano-Bionics, Chinese Academy of Sciences (E1511401). The authors would also like to thank the technical support for Nano-X from Suzhou Institute of Nano-Tech and Nano-Bionics, Chinese Academy of Sciences.

Supporting information

The supporting information is available online at http://chem.scichina.com and http://link.springer.com/journal/11426. The supporting materials are published as submitted, without typesetting or editing. The responsibility for scientific accuracy and content remains entirely with the authors.

References

1 Chen Z, Zhang S, Ren J, Zhang T, Dai J, Wang J, Ma L, Qiao J, Hao X, Hou J. *Adv Mater*, 2024, 36: 2310390
2 Guo C, Fu Y, Li D, Wang L, Zhou B, Chen C, Zhou J, Sun Y, Gan Z, Liu D, Li W, Wang T. *Adv Mater*, 2023, 35: 2304921

3 Shi J, Chen Z, Liu H, Qiu Y, Yang S, Song W, Ge Z. *Adv Energy Mater*, 2023, 13: 2301292
4 Fan B, Gao H, Li Y, Wang Y, Zhao C, Lin FR, Jen AKY. *Joule*, 2024, 8: 1443–1456
5 Sun W, Wang L, Fu Y, Guo C, Zhou J, Chen C, Liu C, Gan Z, Yan K, Li W. *ACS Appl Mater Interfaces*, 2024, 16: 23677–23683
6 Tu S, Zhang L, Lin X, Xiao L, Wang W, Ling Q. *J Mater Chem C*, 2022, 10: 2026–2033
7 Chen Z, Lee MJ, Shahid Ashraf R, Gu Y, Albert-Seifried S, Meedom Nielsen M, Schroeder B, Anthopoulos TD, Heeney M, McCulloch I, Sirringhaus H. *Adv Mater*, 2012, 24: 647–652
8 Zhang Y, Deng J, Mao Q, Young Jeong S, Huang X, Zhang L, Lee B, Huang B, Young Woo H, Yang C, Xu J, Wu F, Cao QY, Chen L. *Chem Eng J*, 2023, 457: 141343
9 Lu J, Wu J, Huang B, Fang Y, Deng X, Zhang J, Chen S, Jeong S, Liu J, Yang C. *Adv Funct Mater*, 2024, 34: 2312545
10 Xu W, Zhang M, Xiao J, Zeng M, Ye L, Weng C, Zhao B, Zhang J, Tan S. *Polym Chem*, 2020, 11: 6178–6186
11 Li Y, Liu J, Shui K, Xie F, Li X, Lin Y, Zhou Z, Zhang Q, Guo F, Li L, Xiao J, Wang M, Ma CQ. *Macromolecules*, 2023, 56: 6276–6289
12 Seo S, Lee J, Kim DJ, Lee D, Phan TN, Park J, Tan Z, Cho S, Kim T, Kim BJ. *Adv Mater*, 2023, 35: 2300230
13 Zheng B, Yue Y, Ni J, Sun R, Min J, Wang J, Jiang L, Huo L. *Sci China Chem*, 2022, 65: 964–972
14 Su W, Zhou X, Yao Z, Bai H, Duan Y, Sun R, Wu Y, Wu Q, Qin H, Zhao C, Zhu W, Woo HY, Min J, Li Y, Ma W, Fan Q. *Adv Funct Mater*, 2024, 34: 2313744
15 Gan Z, Wang L, Cai J, Guo C, Chen C, Li D, Fu Y, Zhou B, Sun Y, Liu C, Zhou J, Liu D, Li W, Wang T. *Nat Commun*, 2023, 14: 6297
16 Wang Z, Wang X, Tu L, Wang H, Du M, Dai T, Guo Q, Shi Y, Zhou E. *Angew Chem*, 2024, 136: e202319755
17 Chen L, Zhao C, Yu H, Sergeev A, Zhu L, Ding K, Fu Y, Ng HM, Kwok CH, Zou X, Yi J, Lu X, Wong KS, Ade H, Zhang G, Yan H. *Adv Energy Mater*, 2024, 14: 2400285
18 Xiao M, Meng Y, Tang L, Li P, Tang L, Zhang W, Hu B, Yi F, Jia T, Cao J, Xu C, Lu G, Hao X, Ma W, Fan Q. *Adv Funct Mater*, 2024, 34: 2311216
19 Pu M, Zhu Y, Tan P, Zhu Y, Lai X, Chen H, Qu J, He F. *Macromolecules*, 2023, 56: 5865–5872
20 Wang M, Cai D, Yin Z, Chen S, Du C, Zheng Q. *Adv Mater*, 2016, 28: 3359–3365
21 Cui Y, Zhu P, Hu H, Xia X, Lu X, Yu S, Tempeld H, Eichel R, Liao X, Chen Y. *Angew Chem Int Ed*, 2023, 62: e202304931
22 Feng G, Li J, He Y, Zheng W, Wang J, Li C, Tang Z, Osvet A, Li N, Brabec CJ, Yi Y, Yan H, Li W. *Joule*, 2019, 3: 1765–1781
23 Lv M, Wang Q, Zhang J, Wang Y, Zhang Z, Wang T, Zhang H, Lu K, Wei Z, Deng D. *Adv Mater*, 2024, 36: 2310046
24 Chen Z, Yao H, Wang J, Zhang J, Zhang T, Li Z, Qiao J, Xiu S, Hao X, Hou J. *Energy Environ Sci*, 2023, 16: 2637–2645
25 Yuan X, Chen H, Kim S, Chen Y, Zhang Y, Yang M, Chen Z, Yang C, Wu H, Gao X, Liu Z, Duan C. *Adv Energy Mater*, 2023, 13: 2204394
26 Wang J, Wang Y, Bi P, Chen Z, Qiao J, Li J, Wang W, Zheng Z, Zhang S, Hao X, Hou J. *Adv Mater*, 2023, 35: 2301583
27 Zhou J, He D, Li Y, Huang F, Zhang J, Zhang C, Yuan Y, Lin Y, Wang C, Zhao F. *Adv Mater*, 2023, 35: 2207336
28 Zhu Y, Guo H, Xiong X, Cai D, Ma Y, Zheng Q. *Adv Mater*, 2024, 36: 2314169
29 Han C, Wang J, Zhang S, Chen L, Bi F, Wang J, Yang C, Wang P, Li Y, Bao X. *Adv Mater*, 2023, 35: 2208986
30 Liu T, Liu J, Li Y, Gao X, Wang M, Zhou Z, He H, Zhang Q, Li L, Huang H, Xiao J, Ma CQ. *ACS Appl Mater Interfaces*, 2024, 16: 50916–50925
31 Huang T, Zhang Z, Liao Q, Wang D, Zhang Y, Geng S, Guan H, Cao Z, Huang Y, Zhang J. *Small*, 2023, 19: 2303399
32 Han Y, Hu Z, Zha W, Chen X, Yin L, Guo J, Li Z, Luo Q, Su W, Ma C. *Adv Mater*, 2022, 34: 2110276
33 Li X, Tang A, Wang H, Wang Z, Du M, Guo Q, Guo Q, Zhou E. *Angew Chem Int Ed*, 2023, 62: e202306847
34 Mei L, Xia X, Sun R, Pan Y, Min J, Lu X, Jen AK, Chen X. *Small*, 2024, 20: 2305977
35 Chen L, Yi J, Ma R, Ding L, Dela Peña TA, Liu H, Chen J, Zhang C, Zhao C, Lu W, Wei Q, Zhao B, Hu H, Wu J, Ma Z, Lu X, Li M, Zhang G, Li G, Yan H. *Adv Mater*, 2023, 35: 2301231
36 Wang M, Liu S, You P, Wang N, Tang G, Miao Q, Yan F. *Sol RRL*, 2020, 4: 2000013
37 Qiu D, Tian C, Zhang H, Zhang J, Wei Z, Lu K. *Adv Mater*, 2024, 36: 2313251
38 He D, Zhou J, Zhu Y, Li Y, Wang K, Li J, Zhang J, Li B, Lin Y, He Y, Wang C, Zhao F. *Adv Mater*, 2024, 36: 2308909
39 Pang S, Chen Z, Li J, Chen Y, Liu Z, Wu H, Duan C, Huang F, Cao Y. *Mater Horiz*, 2023, 10: 473–482
40 Jiang M, Zhi HF, Zhang B, Yang C, Mahmood A, Zhang M, Woo HY, Zhang F, Wang JL, An Q. *ACS Energy Lett*, 2023, 8: 1058–1067
41 Wei Y, Zhou X, Cai Y, Li Y, Wang S, Fu Z, Sun R, Yu N, Li C, Huang K, Bi Z, Zhang X, Zhou Y, Hao X, Min J, Tang Z, Ma W, Sun Y, Huang H. *Adv Mater*, 2024, 36: 2403294
42 Wang H, Lu H, Chen Y, Ran G, Zhang A, Li D, Yu N, Zhang Z, Liu Y, Xu X, Zhang W, Bao Q, Tang Z, Bo Z. *Adv Mater*, 2022, 34: 2105483
43 Zhao B, Chung S, Zhang M, Wei W, Zhu C, Deng C, Cho K, Kan Z. *Adv Funct Mater*, 2024, 34: 2309832
44 Zhu C, Chung S, Zhao J, Sun Y, Zhao B, Zhao Z, Kim S, Cho K, Kan Z. *Adv Sci*, 2023, 10: 2303150
45 Chen X, Huang R, Han Y, Zha W, Fang J, Lin J, Luo Q, Chen Z, Ma C. *Adv Energy Mater*, 2022, 12: 2200044
46 Lin T, Hai Y, Luo Y, Feng L, Jia T, Wu J, Ma R, Dela Peña TA, Li Y, Xing Z, Li M, Wang M, Xiao B, Wong KS, Liu S, Li G. *Adv Mater*, 2024, 36: 2312311
47 Ye L, Hu H, Ghasemi M, Wang T, Collins BA, Kim JH, Jiang K, Carpenter JH, Li H, Li Z, McAfee T, Zhao J, Chen X, Lai JLY, Ma T, Bredas JL, Yan H, Ade H. *Nat Mater*, 2018, 17: 253–260
48 Wang Y, Zhang S, Wang J, Ren J, Qiao J, Chen Z, Yu Y, Hao XT, Hou J. *ACS Energy Lett*, 2024, 9: 2420–2427
49 Zhang L, Hu L, Wang X, Mao H, Zeng L, Tan L, Zhuang X, Chen Y. *Adv Funct Mater*, 2022, 32: 2202103
50 Sang L, Chen X, Fang J, Xu P, Tian W, Shui K, Han Y, Wang H, Huang R, Zhang Q, Luo Q, Ma C. *Adv Funct Mater*, 2023, 33: 2304824
51 Xu L, Xiong Y, Li S, Zhao W, Zhang J, Miao C, Zhang Y, Zhang T, Wu J, Zhang S, Peng Q, Wang Z, Ye L, Hou J, Wang J. *Adv Funct Mater*, 2024, 34: 2314178
52 Lai S, Cui Y, Chen Z, Xia X, Zhu P, Shan S, Hu L, Lu X, Zhu H, Liao X, Chen Y. *Adv Mater*, 2024, 36: 2313105